Highly Photocatalytic Titanium Oxide/Carbon Nitride Heterojunctions Obtained via Dual Asymmetric Centrifugation

Fausthon F. da Silva[1,2*], André L. Menezes de Oliveira[3], Thayná Carla Barbosa de Araújo[4], Luis Fernando Marques-Santos[4], Bo Su[1*]

[1] Biomaterials Engineering, Bristol Dental School, University of Bristol, Lower Maudlin Street, Bristol BS1 2LY, United Kingdom.

[2] Chemistry Department, Federal University of Paraíba (UFPB), 58051-900, João Pessoa – PB, Brazil.

[3] Universidade Federal da Paraíba, Departamento de Química, Núcleo de Pesquisa e Extensão LACOM, 58051-085, João Pessoa, PB, Brazil.

[4] Molecular Biology Department, Federal University of Paraíba (UFPB), 58051-900, João Pessoa – PB, Brazil.

[*]**Corresponding Authors:** fausthon@quimica.ufpb.br (Fausthon F. da Silva) and b.su@bristol.ac.uk (Bo Su).

ABSTRACT

In this work dual asymmetric centrifugation technique was applied to obtain new TiO_2/carbon nitride heterojunctions (TiO_2/g-C_3N_4) with high photocatalytic performance. Materials were obtained from TiO_2 and g-C_3N_4, with an optimal mass ratio of 1.0:0.1 for achieving the highest photocatalytic activity in dyes degradation. The TiO_2/g-C_3N_4 (1.0/0.1) photocatalyst was characterized via X-ray diffraction, confirming the crystalline phases and chemical composition of the material. UV-VIS spectroscopy data showed an increase in the visible light absorption, indicating an effective interaction between the heterojunction components. XPS data showed the formation of Ti^{3+} ions and oxygen vacancies, boosting the photocatalytic process. The TiO_2/g-C_3N_4 (1.0/0.1) showed the highest photocatalytic performance degrading 99.9% of rhodamine B and 99.6% of methylene blue in 60 min under LED light irradiation. Radicals trapping experiments indicated $O_2^{-\bullet}$ radicals as the major photoactive species, through a Z-scheme type mechanism. The product of RhB photodegradation did not show toxicity to *Artemia fransciscana* larvae.

KEYWORDS: Carbon nitride, TiO_2, speed-mixer, dual asymmetric centrifugation, dye photodegradation

1. Introduction

The growth of water disinfection and decontamination technologies is dependent on the development of photocatalytic materials capable of degrading organic pollutants with high efficiency. Among these high-performance materials, titanium dioxide (TiO_2) has stood out as a low-cost, non-toxic, and chemically stable semiconductor with appreciable photocatalytic activity [1]. However, TiO_2 has serious limitations such as large bandgap, poor visible-light absorption, high electro-hole recombination rate and low photogenerated charge separation/migration [2]. Combine TiO_2 with other visible light active semiconductors with narrow band gap to form heterojunctions has emerged as an excellent strategy to boost the photocatalytic performance [1–3]. On the other hand, carbon nitride (g-C_3N_4) is a promising metal-free low-coat photocatalyst, obtained through thermal poly-condensation of many organic molecules such as urea, thiourea and melamine [4,5]. Compared to TiO_2, g-C_3N_4 has an appreciable visible light absorption near 400−460 nm, also showing high thermal stability and high chemical stability in acidic or alkaline medium [4,5]. However, shortcomings low electrical conductivity, low visible light absorption above 460 nm, and especially high charge carriers' recombination rate are still obstacles for practical applications. Several synthetic strategies such as doping have been adopted to improve the g-C_3N_4 photocatalytic properties [6–10]. Thus, the development of g-C_3N_4-based heterojunctions are a viable alternative to improve separation/transfer efficiency of photogenerated electron–hole pairs [4,5].

In this context, TiO_2/carbon nitride (TiO_2/g-C_3N_4) heterojunctions show prominent position in the literature, being applied for photodegradation of dyes, drug-waste, and photoreduction of heavy ions as well [1,2]. Many synthetic strategies have been used to obtain TiO_2/g-C_3N_4 heterojunctions such as simultaneous calcination of the precursors [11,12], loading g-C_3N_4 on the pre-obtained TiO_2 [13,14] or growing TiO_2 crystals over g-C_3N_4 surface [15,16]. Solvent-free methods were also largely applied to form TiO_2/g-C_3N_4 heterojunctions, such as ball-milling [17,18] or manual grinding in a mortar [19,20]. These dry methods provided an environmental-friendly, low cost, fast and practical synthetic routes to obtain highly photoactive heterojunctions. For example, Li and co-workers reported the synthesis of rutile-TiO_2/g-C_3N_4 photocatalyst manually grinding the precursors together for only 10 minutes. This heterojunction was able to totally photodegrade rhodamine B dye (RhB) under simulated sunlight irradiation in 150 minutes [20]. Wang *et. al* also reported the synthesis of TiO_2/g-C_3N_4 heterojunction obtained by ball-milling/microwave method capable to photodegrade 78.27% of RhB and 82.62% of methylene blue (MB) under visible light irradiation in 4 hours [21].

Dual asymmetric centrifugation (DAC), operating in speed-mixer, is a nonconventional and particular type of centrifugation where the vial is turned around the main rotation axis at a fixed distance and also spins around its own centre (a vertical axis) [22]. As a result, the main rotation pushes the sample against the centrifugal force, while the spin movement leads the sample opposite direction [22,23]. This coupled movements reduce the sample´s translational degree of freedom along the central axis, generating a high centrifugal acceleration and very strong shear force, dependent on the frequency of the motion [22,23]. This intense acceleration (700x gravitational force at 3500 rmp) combined with the presence of ceramic beads inside the sample vial, transform this technique a powerful tool to mixer high-viscosity fluids, make homogeneous dispersions, grind powders to a reduced size and synthesized composites [23].

Although it was first used to triturate silver amalgam alloys for dental applications [24], DAC is widely applied for the preparation of lipide-based biomaterials for drug delivery [25], nanocellulose [23], and high-viscosity polymer-based composites [26–29]. Womble and co-workers prepared for the first time TiO_2-based polymeric composite using DAC synthesis, exploring the influence of the nanoparticles on the dielectric properties of polypropylene [27,30]. Alrahlah *et al.* also utilized DAC to produce ZrO_2/TiO_2/PMMA (PMMA = polymethyl methacrylate) composites as dental material for interim restoration applications [31]. Recently, we demonstrated the use of DAC to obtain high-performance S-doped carbon nitride and TiO_2-based photocatalysts, capable of degrading rhodamine B dye in only 60 minutes [32]. Here, we reported the utilization of DAC to synthesize new TiO_2/g-C_3N_4 heterojunctions as photocatalysts. Heterojunctions were synthesized from a commercial P25 TiO_2 and g-C_3N_4 obtained from urea, and characterized by X-ray powder diffraction (XRD), infrared spectroscopy (FT-IR), X-ray photoelectron spectroscopy (XPS), solid-state UV-VIS spectroscopy, scanning electron microscopy (SEM), high-resolution transmission electron microscopy (HRTEM) and energy dispersive X-ray spectra (EDS). Photodegradation of rhodamine B (RhB) and methylene blue (MB) were conducted at room temperature in aqueous solution under visible LED light irradiation. Photocatalytic mechanism was also investigated by radical trapping technique using scavengers. The toxicity of the RhB photodegradation products were investigated using *Artemia* mobility assay.

2. Experimental

Urea (99%), Rhodamine B (RhB, 95%), Ethylenediaminetetraacetic acid (EDTA, 99.4%), p-Benzoquinone (BQ, 98%) and Isopropyl alcohol (IPA, 99.8) were acquired from Sigma-Aldrich. Titanium (IV) oxide (P25) and barium sulphate were purchased from Acros

Organics and Nacalai Tesque INC, respectively. All chemicals were used without previous purification.

2.1. Synthesis of the g-C_3N_4 nanosheets

Bulk g-C_3N_4 was prepared via thermal polymerization of urea at 550 °C for 2 hours and heating rate of 3 °C/min. g-C_3N_4 nanosheets were obtained via thermal exfoliation at 500 °C (10 °C/min) for 2 hours.

2.2. TiO_2/g-C_3N_4 heterojunctions

Titanium oxide nanopowder (Evonik P25, 100 mg) and g-C_3N_4 nanosheet (10 mg) were mixed in a plastic vessel (10 mL) using a SpeedMixer™ (DAC 150.1 FVZ) in 2000 rmp for 30 s. After this period, seven zirconia balls (3 mm diameter) were added to the vessel and the mixture was ground for 2.5 minutes in 2000 rmp (Figure 1). This heterojunction was named TiO_2/g-C_3N_4 (1.0/0.1), indicating the mass ratio between the components. Heterojunctions with other mass proportion were also prepared using the same methodology, and labelled as (1.0/0.3), (1.0/0.5), (1.0/1.0), (0.5/1.0), (0.3/1.0) and (0.1/1.0).

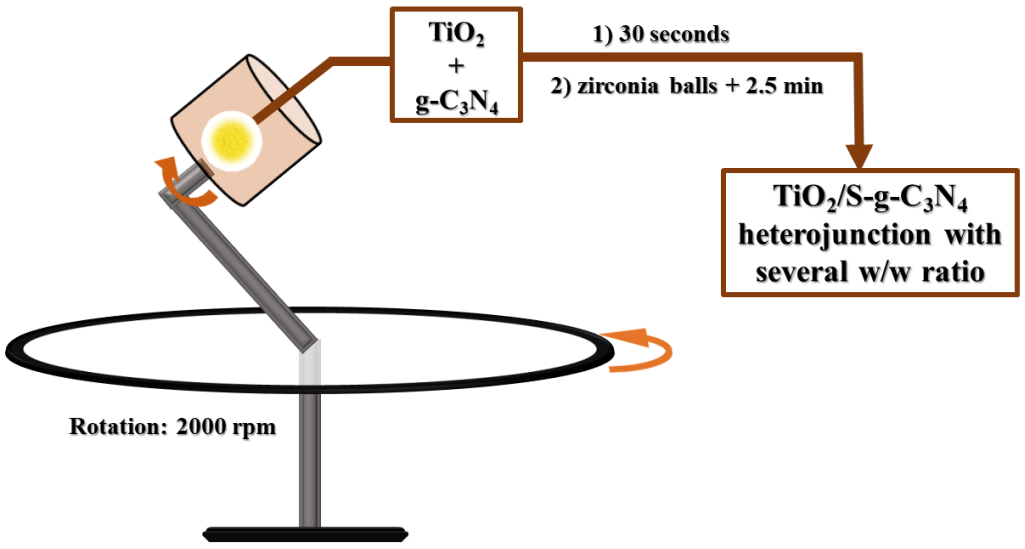

Figure 1: DAC synthesis scheme.

2.3. Characterization

The vibrational spectrum (FT-IR) between 55-4000 cm^{-1} was collected in a PerkinElmer FT-IR spectrometer with an attenuated total reflection attachment (ATR). Powder X-ray diffraction patterns (5-80°) were obtained in a Bruker D8 Advance diffractometer with a PSD

LynxEye detector and Cu radiation (K_α(Cu) = 1.5406 Å), step width 0.02° and acquisition time of 2 s/step. Solid state UV-VIS measurements were performed in a Shimadzu UV-2600 spectrophotometer in absorbance mode using $BaSO_4$ as reference. The surface chemical composition was analyzed by X-ray photoelectron spectroscopy (XPS). The sample was pressed with high purity indium and the spectra was obtained in a Scienta Omicron Argus Analyzer with monochromatic Al K_α X-ray source at 270 W. CasaXPS software was used for spectra deconvolution and data processing. Photoluminescence spectra were recorded in a spectrofluorometer Agilent, Cary Eclipse model, with $e_{xcitation}$ = 350 nm, and excitation/emission slits of 5 nm. The heterojunction morphology was investigated *via* scanning electron microscopy (SEM) and high-resolution transmission electron microscopy (HRTEM) analysis. For SEM, samples were coated with high purity silver and micrographs were acquired in a JSM-IT300 (JEOL, Japan), voltage 15 kV, working distance of 10 mm, using both secondary and backscattered electron detectors. Energy dispersive X-ray spectra (EDS) were collected from a X-max 80 mm^2 (Oxford Instruments, UK). TEM and STEM (HAADF mode) images were collected in a JEM-2100F microscope from JEOL at 200 kV, equipped with an Orius SC1000 camera from Gatan-US. The samples were drop-casted on copper grids which were coated with a thin film (~5 nm) of carbon (high purity graphite), using a Q150 ES from Quorum, USA.

2.4. Photocatalytic assays

Photodegradation investigations were conducted with rhodamine B (RhB) and methylene blue (MB) dyes in aqueous solution (10 ppm and 50 mL). The respective photocatalyst (100 mg) was suspended into the dye solution and kept in the dark under magnetic stirring to achieve adsorption/desorption equilibrium. Then, the solution was irradiated using a blue LED lamp light source (Deltech FD50BL, 50 W, 475-495 nm) positioned vertically 5 cm from the solution. The photodegradation reaction was monitored via UV-VIS spectrophotometry (Shimadzu UV-2600) and the photocatalytic activities were evaluated using the maximum absorbance peak of each dye. Concentrations along the reaction were calculated by Beer-Lambert law, and photodegradation percentages were measured by the following equation:

$$Photodegradation\ (\%) = \frac{C_0 - C_t}{C_0} \quad (\mathbf{1})$$

where C_0 is the concentration before the adsorption/desorption equilibrium and C_t are the concentrations after each 30 minutes of irradiation. Radicals trapping technique was employed

to investigate the photocatalytic mechanism using the same experimental procedure, except by the addition of isopropyl alcohol (IPA, $6.4x10^{-1}$ mol/L), EDTA ($6x10^{-4}$ mol/L) and p-benzoquinone (BQ, $2x10^{-3}$ mol/L), for scavengers of hydroxyl radicals, photogenerated holes and superoxide radicals, respectively [32].

2.5 Artemia culture and toxicity test

Artemia survival/mobility assays has been used to investigate the toxic effect of photodegraded RhB[33]. For this purpose, cysts of *Artemia franciscana* were obtained from Artemia International LLC (Texas, USA; hatching rate 90%). For nauplii hatching, cysts (10 mg) were placed in Petri dishes containing artificial seawater (ASW) for 24 h (25 ± 1 °C; 3000 - 4000 lumens). Hatched nauplii at instar I stage were transferred to Petri dishes containing fresh ASW and cultured for additional 24 h (25 ± 1 °C; dark) until the instar II stage [34].

Nauplii at instar II stage (10 larvae/well; 2 mL ASW/well; 24-well plates) were exposed to different concentrations of untreated and photodegraded RhB (4, 8, 16, 24 and 32 ppm). Larvae mobility was used as toxicity endpoint and was analysed 24 h and 48 h post-exposure under light microscope [34]. Larvae were classified as immobile if they did not exhibit any swimming behavior for longer than 10 s of observation [35]. The control group was cultured in Milli-Q® water (80%) plus ASW (20%) since pure Milli-Q® water (100%) was toxic for *A. franciscana*. Serial dilutions of untreated RhB and photodegraded RhB were prepared using Milli-Q® water supplemented with 20% of ASW.

Mobility percentages were calculated by the following equation:

$$Mobility\ (\%) = \frac{S - I}{S}\ x\ 100 \quad (\mathbf{2})$$

where S is the number of swimming larvae, and I is the number of immobile larvae. The experiments were carried out in triplicate (technical replicate) and repeated four times in an independent manner (biological replicate).

3. Results and Discussion

Pure g-C_3N_4 was obtained through thermal polymerization of urea. XRD pattern (Figure S1) shows the main signal at 27.57° related to the (002) diffraction plane due to interlamellar aromatic π-π stacking interactions, typical of graphite-like materials. This corresponds to an interlayer distance of 0.32 nm, in agreement with the literature [36]. The signal regarding to the (100) diffraction plane was also observed at 12.95° and d-spacing of 0.68 nm, corresponding to the intralayer distance [36]. DAC was employed to obtain TiO_2/g-C_3N_4 heterojunctions with

different mass ratio, however, since they are similar, only the characterization of sample with mass ratio (1.0/0.1) was reported here due to its superior photocatalytic activity. The X-ray diffraction pattern of TiO_2/g-C_3N_4 (1.0/0.1) (Figure 2 (a) blue line) shows the typical 2θ values for anatase (ICSD 082082) and rutile (ICSD 085492) crystalline phases. The most intense signal for each phase is at 25.6° and 27.720°, related to the (101) and (110) diffraction planes of anatase and rutile, respectively.

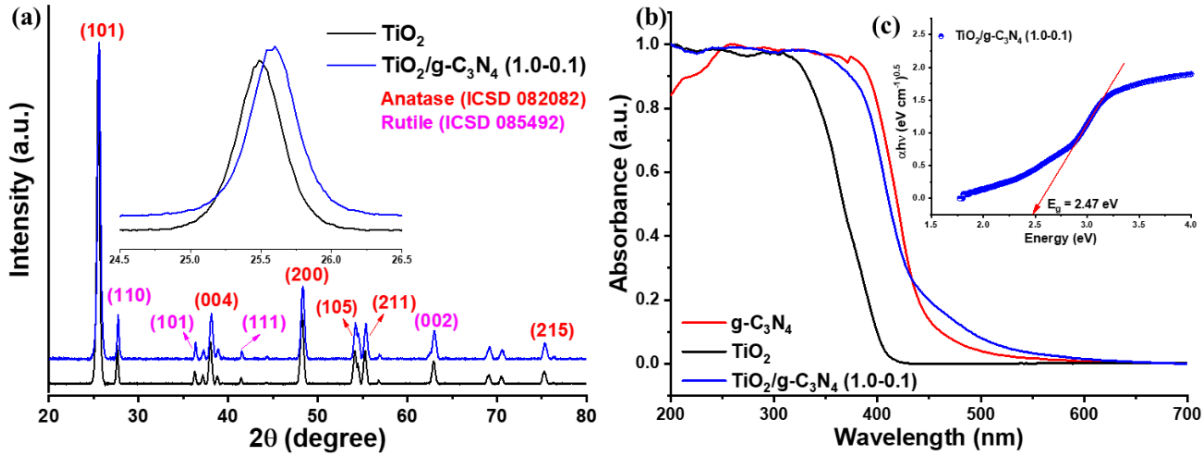

Figure 2: (a) Experimental powder pattern of pure TiO_2 (black line) and TiO_2/g-C_3N_4 (1.0/0.1), highlighting the shifts in the XRD signal (insert). (b) Solid-state UV-VIS absorption spectra of the precursors, TiO_2/g-C_3N_4 (1.0/0.1) (blue line) and (c) Tauc plot for the heterojunction.

Crystallite sizes were estimated by Scherrer' equation:

$$D = \frac{K\lambda}{\beta cos\theta} \qquad (3)$$

where D is the crystallite size, K is the shape factor (≈ 0.90), λ is the K_α wavelength of the Cu radiation source (1.5406 Å) and β is the full width at half maximum (FWHM) of each individual peak and θ is the Bragg's angle. Considering the first eight signals, D values of 22.58 nm and 23.83 nm were obtained, respectively for TiO_2/g-C_3N_4 (1.0/0.1) and the pure TiO_2. This decrease in the crystallite size can be justified by the grinding process during the DAC synthesis. As expected, no signals related to the g-C_3N_4 were observed due to its low content, in agreement with similar systems in the literature [21,32]. On the other hand, the main vibrational bands of g-C_3N_4 can be observed in Figure S2, due to its strong absorption in the infrared region compared to TiO_2. The band centered at 3336 cm^{-1} corresponds to the asymmetric N-H and O-H stretching of g-C_3N_4 terminal amine groups and hydroxyl groups on

the metal oxide surface. Signals at 1604 cm^{-1} and 1029 cm^{-1} are due to the C-N/C=N stretching of the heptazine rings (C_6N_7), while the signal regarding the triazine ring (C_3N_3) are located at 1420 cm^{-1}. Signals related to the asymmetric C-H stretching (2907 cm^{-1}), asymmetric Ti-O stretching (600 cm^{-1}) and N-H bending (883 cm^{-1}) are also observed. All signals observed agrees with similar heterojunctions in the literature [37–41].

UV-VIS solid-state absorption spectra of TiO_2 (black line), g-C_3N_4 (red line) and TiO_2/g-C_3N_4 (1.0/0.1) (blue line) are shown in Figure 2 (b). An improvement in the visible light absorption of the heterojunction was observed compared to the pure TiO_2, red shifting the maximum absorption peak. TiO_2/g-C_3N_4 (1.0/0.1) also shows a higher absorption at $\lambda > 450$ nm compared to the pure g-C_3N_4, extending the absorption far in the visible region and favoring the photocatalytic activity. Li *et al.* also observed this phenomenon for rutile-TiO_2/g-C_3N_4 heterojunction obtained by manual grinding method in a mortar [20]. Other heterojunctions with higher visible absorption compared to the pure g-C_3N_4 were also obtained by hydrothermal [11], simultaneous calcination [14] and impregnation [42,43] methods. The materials' bandgaps (E_g) were calculated by Tauc plot using the following equation:

$$(\alpha h\nu)^n = A\left(h\nu - E_g\right) \qquad (\mathbf{4})$$

where A is a constant, and α, h, and ν are the absorption coefficient, Plank's constant and the photon frequency, respectively. Considering TiO_2 and g-C_3N_4 as semiconductors with direct and indirect bandgap (n = 0.5 or n = 2) [44,45], E_g values were 3.25 eV and 2.63 eV, respectively (Figure S3 and S4). For the TiO_2/g-C_3N_4 (1.0/0.1) heterojunction (Figure 2 (c)), the estimated E_g was 2.47 eV, because of the improvement in the absorption in visible region. This reduction in the bandgap compared to the pure g-C_3N_4 was also noticed by Li and co-workers in the heterojunctions synthesized through impregnation in methanol solution [42] and by Ma *et al.* in heterojunctions obtained by growing TiO_2 crystals on the g-C_3N_4 surface [46].

Surface chemical composition of the TiO_2/g-C_3N_4 (1.0/0.1) heterojunction and the precursors were investigated via XPS. Carbon 1s XPS spectrum (Figure S5) for pure g-C_3N_4 shows signals at 285.9, 286.9 and 291.3 eV, due to the presence of the C=C, C-N-C and N-C=N organic groups of heptazine and triazine motifs, respectively [32,47]. N1s spectrum (Figure S5) also confirms the signals related to the main nitrogenated groups -C=N-C- (396.4 eV), -NC_3 (398.2 eV) and -NH_2 (402.3 eV). O 1s and Ti 2p high-resolution XPS spectra for pure TiO_2 are shown in Figure S6. Deconvolution for oxygen 1s spectrum indicates the presence of lattice oxygen (530.44 eV) and oxygen vacancies (531.76 eV). Quantitatively (Table S1), oxygen vacancies represent 9.93% on the TiO_2 surface, with the remaining percentage (90.07%) corresponding to lattice oxygen atoms. Thus, the presence of oxygen vacancies leads to the

reduction of Ti^{4+} → Ti^{3+} on the oxide surface, as confirmed by the presence of signals at 456.97 eV (Ti $2p_{3/2}$) and 461.28 eV (Ti $2p_{1/2}$) of the Ti^{3+} ions (Figure S6), in agreement with other reports in the literature [48,49]. The majority presence of Ti^{4+} ions in pure TiO_2 was confirmed by the peaks near 464.88 eV (Ti $2p_{1/2}$) and 459.16 (Ti $2p_{3/2}$), with concentration of 97.80% (Table S1), far larger than Ti^{3+} (2.20%), agreeing with the low content of oxygen vacancies.

For TiO_2/g-C_3N_4 (1.0/0.1), the survey spectrum (Figure S7) reveals the presence of Ti, O, C and N, as expected. The largest percentage of the material surface is composed of oxygen (45.67%) and titanium (32.43%) atoms, in accordance with the higher TiO_2 content in the sample compared to g-C_3N_4 (Table 1). The Ti 2p high-resolution spectrum (Figure 3(a)) was deconvoluted into three peaks at 459.21eV (Ti^{4+} $2p_{3/2}$), 464.89 eV (Ti^{4+} $2p_{1/2}$) and 462.82 (Ti^{3+} $2p_{1/2}$). The intense energy used in the DAC synthesis process led to more intense reduction of Ti^{4+} ions, increasing the percentage of Ti^{3+} from 2.20% to 9.70% on the surface (Table S2). For O 1s high-resolution XPS spectrum (Figure 3(b)) an intense signal at 530.42 was noticed, related to the lattice oxygen atoms into the TiO2 structure. Additionally, the increase in the percentage of oxygen vacancies in the composite (19.40%, Table S3 and Figure 3(b)) was also observed. Thus, high energy in the grinding process can lead to a recombination of oxygen atoms in the surface to form O_2, reducing metal ions and generating oxygen vacancies. This process is summarized in the following equation using Kröger-Vink notation.

$$2Ti_{Ti}^{x} + O_{O}^{x} \rightarrow 2\,Ti_{Ti}^{\prime} + V_{0}^{\bullet\bullet} + \frac{1}{2}O_{2(g)} \quad (\mathbf{5})$$

Deconvolution of carbon 2p spectrum (Figure 3(c)) indicates the presence of three peaks at 284.9 eV, 285.3 eV, 289.0 eV, corresponding respectively to C=C, C-N-C and N-C=N organic groups of heptazine and triazine motifs into the g-C_3N_4. For N 1s spectrum (Figure 3(d)), two signals at 399.2 eV and 400.3 eV were observed, related to C=N-C and N-C_3 organic groups in the g-C_3N_4. The binding energy shifts observed in the Ti 2p, C 1s and N 1s spectra demonstrate the formation of the heterojunction, as well as an effective interaction and charge migration between the components, as observed in similar to other TiO_2/g-C_3N_4 composites in the literature [11–17,42,43,50].

Table 1: XPS survey deconvolution parameters for TiO_2/g-C_3N_4 (1.0/0.1) heterojunction.

Element	Position (eV)	FWHM	Area	Atomic percentage (%)
Ti 2p	451.50	2.19	2877.9	32.43
O 1s	530.50	1.51	1520.3	45.67
C 1s	285.00	1.63	220.4	19.40
N 1s	399.50	1.76	51.1	2.50

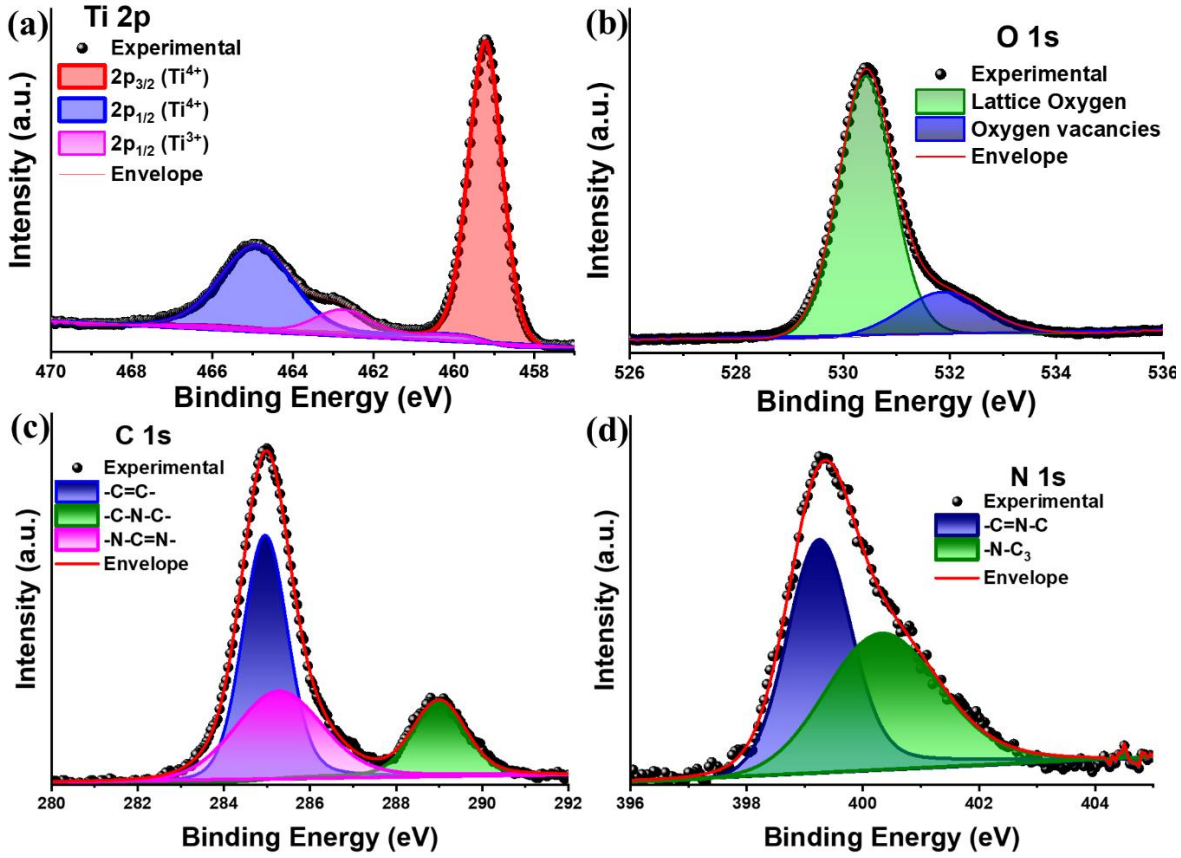

Figure 3: High-resolution XPS spectra of (a) Ti 2p, (b) O 2p, (c) C 2p and (d) N 2p for TiO_2/g-C_3N_4 (1.0/0.1) heterojunction.

The efficiency in separating the photogenerated charges was investigated using solid-state photoluminescence spectroscopy at room temperature, and the results are shown in Figure S8. Under excitation at 350 nm, the free g-C_3N_4 presents a broad blue emission band centered at 460 nm (Figure S8, red line). According to Zhang and co-workers, this typical blue emission is related to the electronic transitions between lone pair (LP) states in valence band and the π* antibonding states in conduction band [51]. TiO_2/g-C_3N_4 (1.0/0.1) heterojunction also exhibits a large emission band, blue-shifted by 16 nm (Figure S8, blue line). The heterojunction

formation also led to a significant decrease in photoluminescence intensity, indicating a decrease in the recombination processes of photogenerated charges [18,21,47], boosting the photocatalytic performance.

Morphological investigations of the TiO_2/g-C_3N_4 (1.0/0.1) heterojunction reveal the presence of high aggregated particles (Figure 4(a)), like other samples prepared through mechanical methods *e.g.*, ball milling [18,21,38,47]. TEM images (Figure 4(b) and S9) indicate a distribution of TiO_2 nanoparticles on the g-C_3N_4 nanosheet surface, also confirmed by the presence of the (101) diffraction plane of TiO_2 with d-spacing 0.356 nm (Figure 4(c)), similar to the one found in the literature [21,47] and near the value obtained in the XRD data (0.350 nm). The TiO_2 particle size distribution (Figure 4(d)) shows a mean size of 22.67 nm, consistent with the crystallite size obtained by experimental diffraction patterns. EDS mappings (Figure 4(e-h)) confirm the Ti, O, C and N elemental composition and the presence of TiO_2 nanoparticles on the surface of the carbonaceous material. However, the high content of carbon and nitrogen around the TiO_2 nanoparticles (Figure 4(g and h)) can also be noticed. More detailed elemental mappings of TiO_2 nanoparticles (Figure S10) confirm the presence of a g-C_3N_4 covering (≈ 6.5 nm thickness) around the TiO_2 nanoparticles, similar to other works in literature [17].

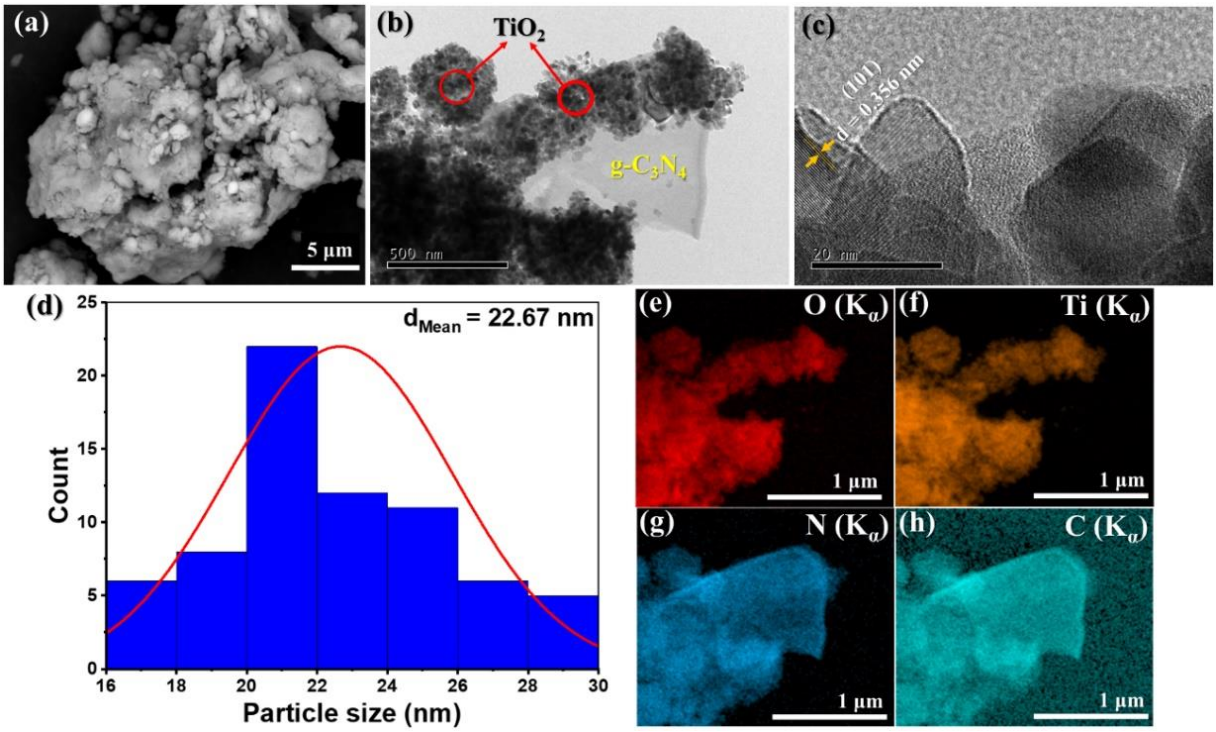

Figure 4: (a) SEM and (b,c) HRTEM imagens, (d) particle size distribution and (e-h) EDS mapping of O, Ti, N and C of TiO_2/g-C_3N_4 (1.0/0.1) heterojunction.

Photocatalytic performance of the TiO_2/g-C_3N_4 heterojunctions for the degradation of RhB and MB dyes were investigated compared to the pure precursors. For RhB, the system was left until the adsorption/desorption equilibrium for 30 minutes (Figure 5(a)), resulting in adsorption uptakes between 38.9-13.8% (Table S4) with the high value for the TiO_2/g-C_3N_4 (1.0/0.1), may indicate higher surface area and higher RhB affinity of this heterojunction compared to the others. For the pure TiO_2 and g-C_3N_4, the adsorption percentages were 5.17% and 20.1%, respectively, suggesting that DAC synthesis improves the materials' surface area for TiO_2/g-C_3N_4 mass ratio ≥ 1. After light was on, RhB started to photodegrade, indicated by the decreasing in the absorption bands and concentrations (Figure 5(a) and S8). The dye absorption bands profile during the photocatalytic process (Figure S11) indicates a degradation pathway via *N*-deethylation process as observed before for similar photocatalysts [32,52,53]. The heterojunctions degradation profile and percentages are shown Figure 5(b,c) and Table S4, showing the TiO_2/g-C_3N_4 (1.0/0.1) with the highest photocatalytic performance, degrading 99.9% of RhB in 60 minutes of irradiation. All heterojunctions show superior photocatalytic activity compared to the pure TiO_2 (59.1%, Figure S12) and the TiO_2/g-C_3N_4 (1.0/0.1) sample also has higher performance than the free g-C_3N_4 (97.8%, Figure S13). The moderate photocatalytic activity of TiO_2 can be explained dye-sensitized energy transfer mechanism, due to the presence of RhB on the metal oxide surface [54].

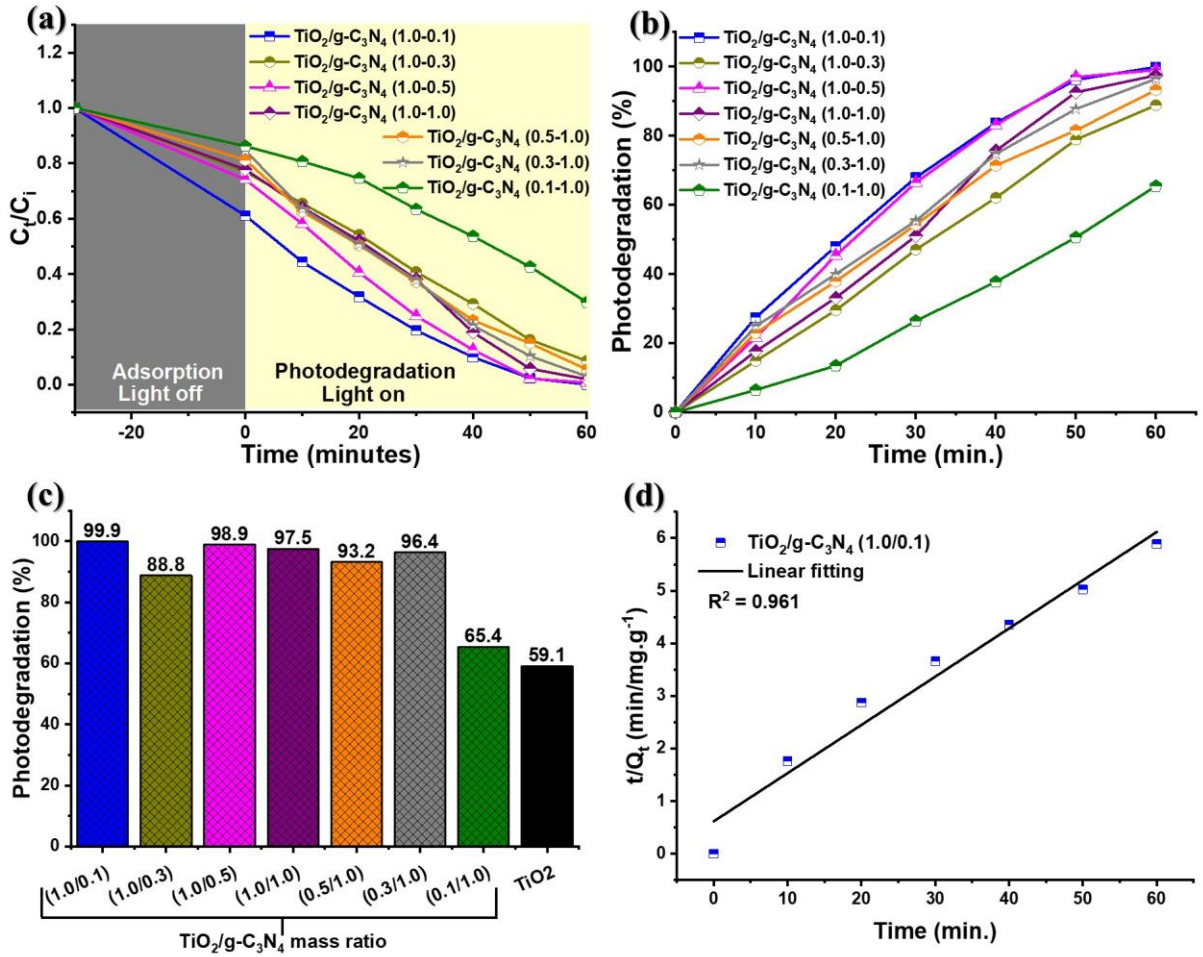

Figure 5: (a) C_t/C_i ratio with decreasing in the RhB concentration during adsorption and photodegradation processes, (b) photodegradation profile and (c) degradation percentages of the heterojunctions, and (d) Pseudo-second order plot of the TiO_2/g-C_3N_4 (1.0/0.1).

From the TiO_2/g-C_3N_4 (1.0/0.1) photodegradation data, the reaction kinetics were investigated, and result is shown in Figure 5(d). The experimental data agree with the pseudo-second order model, when the reaction rate is dependent on the amount of the solute adsorbed on the photocatalyst surface and the amount adsorbed at equilibrium, as described by the equation (5):

$$\frac{t}{Q_t} = \frac{1}{k_2 Q_e^2} + \frac{t}{Q_e} \qquad (6)$$

where t, Q_t, Q_e and k_2 are the time, amount of dye adsorbed at each time, amount of dye adsorbed at the equilibrium and the pseudo-second order reaction rate, respectively [55,56]. Pseudo-second order kinetic models were also used to describe photocatalytic and adsorption properties of other carbon nitride-based materials in literature [57–59]. Pure TiO_2 follows a

pseudo-first order kinetic model as shown in the Figure S12, commonly found for several photocatalysts in the literature including TiO_2/g-C_3N_4 systems [17,21,37]. However, the photodegradation of RhB in the presence of pure g-C_3N_4 also fits well with the pseudo-second order model, as shown in Figure S13. Clearly, the TiO_2/g-C_3N_4 (1.0/0.1) heterojunction presents superior performance compared with the pure precursors. Table 2 shows results of the photocatalytic performance of TiO_2/g-C_3N_4 (1.0/0.1) sample in the RhB photodegradation, compared to the other heterojunctions with similar compositions and obtained through different synthesis methods. The photocatalyst obtained here shows similar or superior activity, as observed, indicating the DAC technique as a promising method to obtain high photoactive heterojunctions.

Table 2: Photocatalytic activity of TiO_2/g-C_3N_4-based heterojunctions in the degradation of RhB.

Photocatalyst	Synthesis method	Degradation (%)	Time (min)	Light source	Ref.
TiO_2/g-C_3N_4 (1.0-0.1)	**DAC**	**99.9**	**60**	**50 W blue LED**	**This work**
N–TiO_2/g-C_3N_4	grinding	98.8	35	800 W Xe lamp with a UV cut-off filter	[37]
rutile-TiO_2/g- C_3N_4	grinding	99	150	500 W Xe lamp	[20]
g- C_3N_4/TiO_2	ball milling	78.27	240	500 W Xe lamp with UV cut-off filter	[21]
g-C_3N_4/TiO_2	ball milling	99.41	120	60 W, 460 nm lamp	[60]
Ti^{3+}-TiO_2/O-g-C_3N_4	hydrothermal	99	100	30 W LED cold visible light	[61]
g-C_3N_4/TiO_2	hydrothermal	80	300	500 W Xe lamp UV-cut off filter (365 nm)	[62]
mTiO_2_ex-C_3N_4	hydrothermal	100	540	150 W halogen lamp with UV-cut off filter (400 nm)	[63]
g-C_3N_4/TiO_2	hydrothermal	100	10	300 W Xe lamp	[64]
g-C_3N_4/reduced TiO_2	hydrothermal	88.6	90	350 W Xe lamp UV-cut off filter (420 nm)	[65]
TiO_2 nanorods/g-C_3N_4 nanosheets	hydrothermal	99.9	12	300 W Xe lamp	[66]
TiO_2/g- C_3N_4 nanosheets	hydrothermal	99.9	60	500 W Xe lamp	[67]
TiO_2/Graphitic Carbon Nitride Nanosheets	impregnation in solution	100	10	500 W Xe lamp	[68]
core-shell TiO_2@g- C_3N_4	impregnation in solution	93.3	100	300 W Xe lamp with a UV-cut off filter (420 nm)	[69]

g-C_3N_4@TiO_2 hollow microspheres	impregnation in solution	90.8	90	350 W Xe lamp	[70]
g-C_3N_4/TiO_2 with exposed (001)	impregnation in solution	55	300	300 W halogen lamp	[71]
g-C_3N_4-TiO_2	impregnation in solution	99	20	500W Xe lamp	[72]
TiO_2 hollow sphere/g-C_3N_4	Impregnation in solution	98.1	120	250 W Xe lamp with UV-cut off filter (420 nm)	[73]
2D/2D g-C_3N_4/TiO_2 with exposed (001)	Impregnation in solution	99	120	500 W Xe lamp	[74]

Photocatalytic performance of the TiO_2/g-C_3N_4 (1.0/0.1) heterojunction for degradation of methylene blue (MB) was also investigated (Figure 6 and S14), compared to the free precursors (Figure S15-17). The systems achieved the adsorption/desorption equilibrium after 60 minutes with MB uptake of 1.5%, 22.3% and 21.5% for TiO_2, g-C_3N_4 and TiO_2/g-C_3N_4 (1.0/0.1), respectively. After irradiation, the MB concentration decreased in the presence of all photocatalysts (Figures 6(a), S15 and S16), and the blueshifts observed in the main absorption band at 664 nm indicate that photodegradation follows a mechanism via loss of dimethylamino groups [75]. As shown in Figures 6(b) and (c), the TiO_2/g-C_3N_4 (1.0/0.1) heterojunction shows the highest photodegradation percentage (99.6%) in 150 minutes, compared to pure TiO_2 (60.1%) and pure g-C_3N_4 (84.4%).

In opposition to the RhB photodegradation, both precursors present reaction kinetics consistent with a pseudo-first order model, as observed in Figures S17 and S18. Nonetheless, the experimental data of the TiO_2/g-C_3N_4 (1.0/0.1) heterojunction also agrees with a pseudo-second order kinetic reaction, as observed for RhB photodegradation. (Figure 6(d)). Table 3 shows the MB photodegradation and reaction time values for several TiO_2/g-C_3N_4 based photocatalysts, compared to those ones obtained in this work. The TiO_2/g-C_3N_4 (1.0/0.1) heterojunction presents photocatalytic performance equal to or superior to the other photocatalysts with a lower power visible light source, when compared to light sources conventionally used in the literature (300 W Xe lamp). In general, higher photodegradation reaction times for MB were observed in the literature, compared to those found for the degradation of RhB. However, the reaction time obtained for the TiO_2/g-C_3N_4 (1.0/0.1) heterojunction in the total degradation of MB (120 minutes) is far inferior to other catalysts of similar composition.

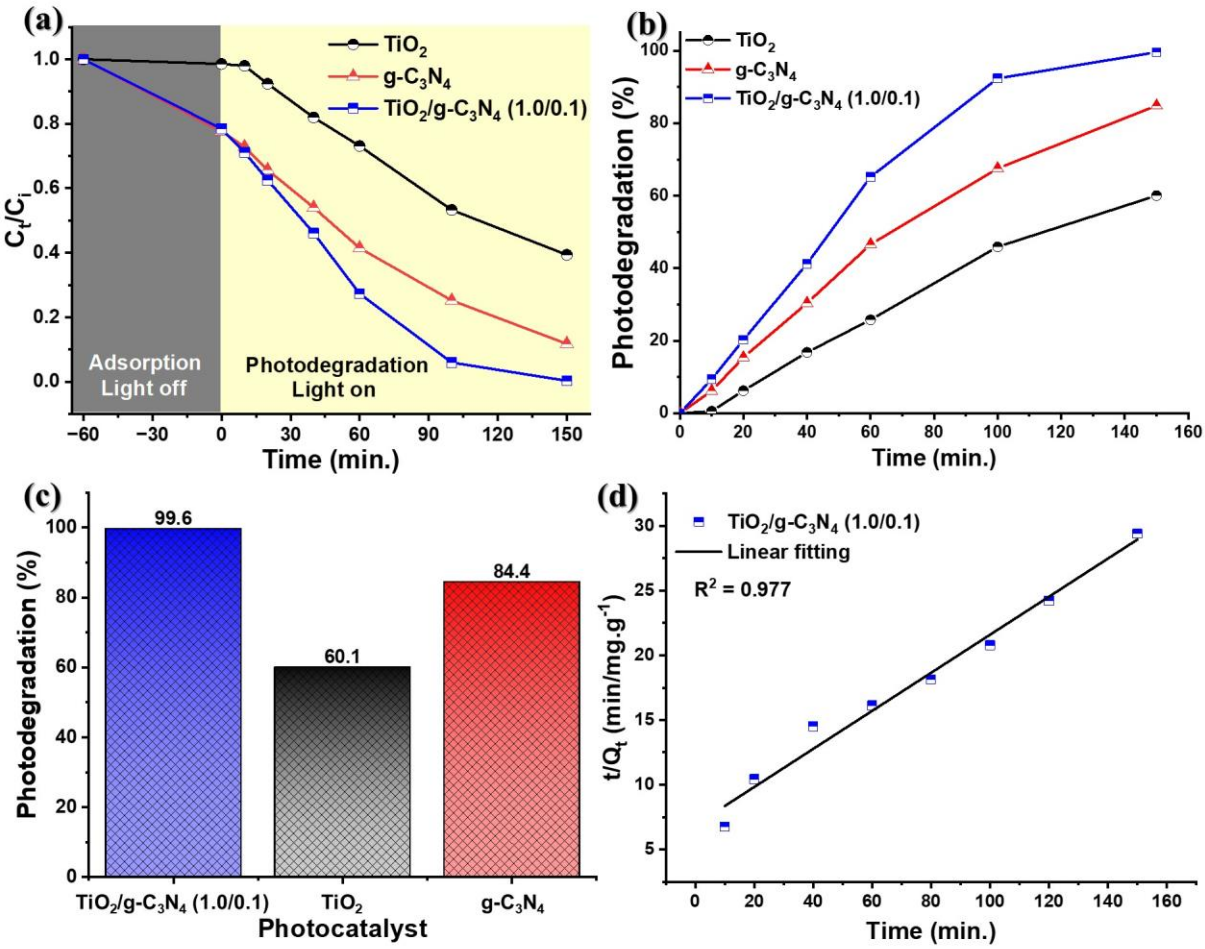

Figure 6: (a) C_t/C_i ratio with decreasing in the MB concentration during adsorption and photodegradation processes, (b) photodegradation profile and (c) degradation percentages of TiO_2/g-C_3N_4 (1.0/0.1) compared to the precursors, and (d) Pseudo-second order plot of the TiO_2/g-C_3N_4 (1.0/0.1).

Table 3: Photocatalytic activity of TiO_2/g-C_3N_4-based heterojunctions in the degradation of MB.

Photocatalyst	Degradation (%)	Time (min)	Light source	Ref.
TiO_2/g-C_3N_4 (1.0-0.1)	**99.6**	**150**	**50 W blue LED**	**This work**
g-C_3N_4/TiO_2	82.62	120	300 W Xenon lamp with a cut-off filter ($\lambda > 420$ nm)	[21]
g-C_3N_4/TiO_2 films	68	180	50 W Halogen lamp with a cut-off filter ($\lambda > 400$ nm)	[76]
g-C_3N_4/TiO_2	91	360	500W Xenon lamp with a cut-off filter ($\lambda > 400$ nm)	[77]
g-C_3N_4/TiO_2	98	100	100 W Halogen lamp with a cut-off filter ($\lambda > 400$ nm)	[78]

Na-g-C_3N_4/TiO_2	90	75	300 W Xenon lamp with a cut-off filter ($\lambda > 400$ nm)	[79]
N/Ti^{3+}-codoped triphasic g-C_3N_4/TiO_2	81.64	100	Xenon lamp with a cut-off filter ($\lambda > 420$ nm)	[80]
Mesoporous TiO_2/g-C_3N_4 nanocomposite	96	90	400 W visible lamp	[81]
g-C_3N_4/TiO_2	94	150	300 W Xenon lamp with a cut-off filter ($\lambda > 420$ nm)	[82]
mpg-C_3N_4/anatase TiO_2	64	360	500 W Xenon lamp	[83]
TiO_2/g-C_3N_4	100	330	15 W of UV-B lamps	[84]
g-C_3N_4/TiO_2 nanotube	81	180	Xenon lamp with a cut-off filter ($\lambda > 420$ nm)	[85]
g-C_3N_4/TiO_2 nanocomposite	100	120	300 W halogen lamp with a UV cut-off filter	[86]
Ti^{3+} Self-Doped TiO_2/g-C_3N_4	99	100	30 W LED visible light	[87]
TiO_2/g-C_3N_4	73	80	250 W Xenon lamp with a cut-off filter ($\lambda > 420$ nm)	[88]
g-C_3N_4/N-TiO_2	65	80	500 W Xenon lamp with a cut-off filter ($\lambda > 420$ nm)	[89]
g-C_3N_4/C–TiO_2	99	150	400 W Xenon lamp with a cut-off filter ($\lambda > 420$ nm)	[90]
g-C_3N_4/TiO_2	95	360	500W Xenon lamp with a 420 nm cut-off filter	[91]
g-C_3N_4/TiO_2	91.75	120	60 W lamp (460 nm)	[60]

Radical trapping technique was applied to investigate the RhB photocatalytic mechanism of the TiO_2/g-C_3N_4 (1.0/0.1), using BQ, IPA and EDTA as scavengers for $O_2^{-\bullet}$, $HO^\bullet$ and h^+, respectively. Results in Figure S19 show a photodegradation of 34%, 68.6% and 81.2%, respectively when scavengers of superoxide radicals, hydroxyl radicals and holes were applied. Thus, experimental data indicate that the three photogenerated species ($O_2^{-\bullet}$, $HO^\bullet$ and h^+) have influence on the RhB degradation process, however the major photocatalytic mechanism is through the formation of superoxide radicals, followed by the $HO^\bullet$ radicals. Since the formation of photogenerated species is related to the energetic position of the valence (E_{VB}) and conduction bands (E_{CB}), Valence Band XPS (VB-XPS) measurements were conducted in order to obtain the energy diagram, seeking a better understanding of the photocatalytic mechanism.

The experimental potentials for the valence band of pure TiO_2 and g-C_3N_4 obtained (Figure S20-21) were converted to standard hydrogen potential ($E_{VB\text{-}NHE}$) through the equation (6) [92]:

$$E_{VB-NHE} = \varphi + E_{VB-XPS} - 4.44 \quad (7)$$

where φ is XPS analyzer work-function (4.55 eV) and $E_{VB\text{-}XPS}$ is the potential obtained from the VB-XPS spectrum, being 3.127 eV and 0.337 eV for TiO_2 and g-C_3N_4, respectively. The energy positions of the valence band (E_{VB}) were +3.24 eV and +0.45 eV for TiO_2 and g-C_3N_4, respectively. Considering the experimental E_g values obtained from the UV-VIS data the conduction band energy positions (E_{CB}) for TiO_2 and g-C_3N_4 were +0.40 eV and -2.18 eV, respectively.

Since $O_2^{-\bullet}$ and $HO^{\bullet}$ radicals play the most important role in the photocatalytic degradation of RhB (Figure S19), it is possible to investigate the formation of theses photogenerated species, bearing in mind that the superoxide radicals are obtained by reduction of atmospheric O_2 ($E°(O_2/O_2^{-\bullet})$ = -0.33 eV) by the electrons at conduction band (CB) and hydroxyl radicals are formed by water ($E°(H_2O/HO^{\bullet})$ = +1.99 eV) or hydroxyl ions oxidation ($E°(OH^-/HO^{\bullet})$ = +2.72 eV) through the holes at the valence band (VB) of the materials. Notoriously, the $O_2^{-\bullet}$ radicals are the main photoactive species during the RhB degradation, however, these radicals only can be formed at the g-C_3N_4 conduction band (E_{CB} = -2.18 eV) due to its higher negative potential. In addition, comparing the E_{VB} positions of TiO_2 (+3.24 eV) and g-C_3N_4 (+0.45 eV), high h^+ concentration must be positioned at VB of TiO_2 to generate $HO^{\bullet}$ radicals from water molecules and/or hydroxyl ions [52]. Holes preferentially positioned in the TiO_2 valence band can also contribute to the direct oxidation of RhB, however, the trapping experiments results (Figure S19) indicate this as a less favored pathway when compared to the dye oxidation via superoxide and hydroxyl radicals.

Therefore, considering the results observed and the E_{VB} and E_{CB} energy positions of the materials, the electrons must be preferentially positioned at the CB of the g-C_3N_4, and holes must be preferentially located in the VB of TiO_2, and these observations are compatible with a Z-scheme type mechanism (Figure 7). In this case, there is a selective recombination between holes located in the VB of g-C_3N_4 and electrons located in the CB of TiO_2. This results in the remaining photogenerated charges located in the higher positive VB and in the more negative CB, favoring a high photocatalytic performance. These results are similar to the photodegradation mechanism found for other TiO_2/g-C_3N_4 based materials [20,21,32,64,74].

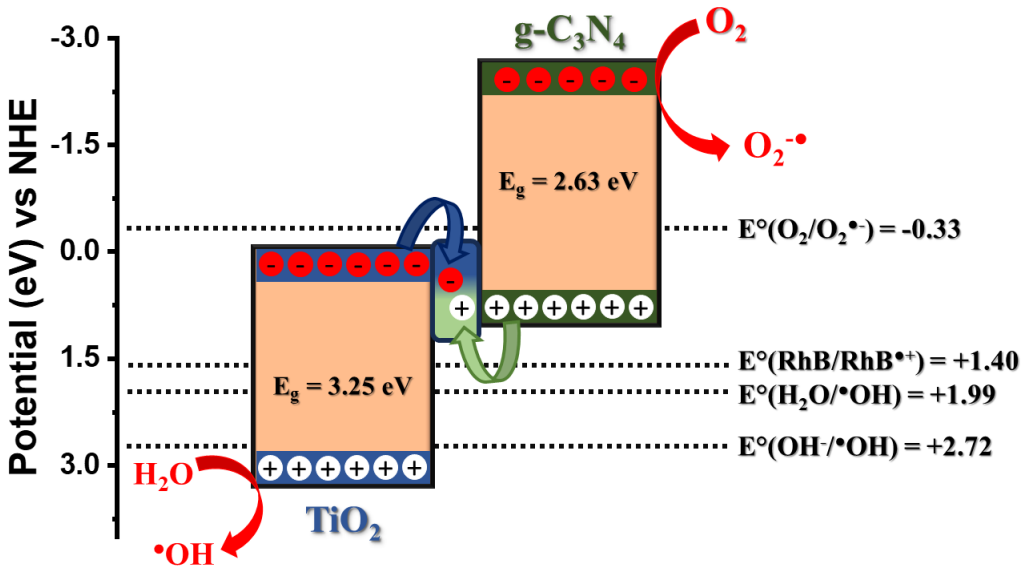

Figure 7: Z-scheme mechanism in the photodegradation of RhB in the presence of TiO_2/g-C_3N_4 (1.0/0.1) photocatalyst.

Artemia toxicity test has been widely used to evaluate the harmful effect of several compounds - from pharmaceutical drugs to environmental contaminants - to the biological systems [93,94]. Our experimental protocol intended to evaluate two different stages of *Artemia franciscana* development: instar II (24 h of exposure) and instar III (48 h of exposure), being the last the most sensitive to toxic compounds [34,95]. Our results showed that photodegraded RhB did not exhibit deleterious effect on *A. franciscana* larvae even after 48 h of exposure for all concentration tested (Figure 8(b); compared to the control group; Kruskal-Wallis test). No difference was found in larvae mobility after exposure to untreated RhB or photodegraded RhB. The mobility rates at the highest concentration tested were 88.3 $\pm$ 3.66% and 80 $\pm$ 4.77% (mean $\pm$ SEM; untreated RhB and photodegraded RhB, respectively; 32 ppm; 48 h of exposure; Kruskal-Wallis test). So, our data strongly suggests that no toxic compounds were produced as result of RhB photodegradation by TiO_2/g-C_3N_4, pointing out the method as a safe.

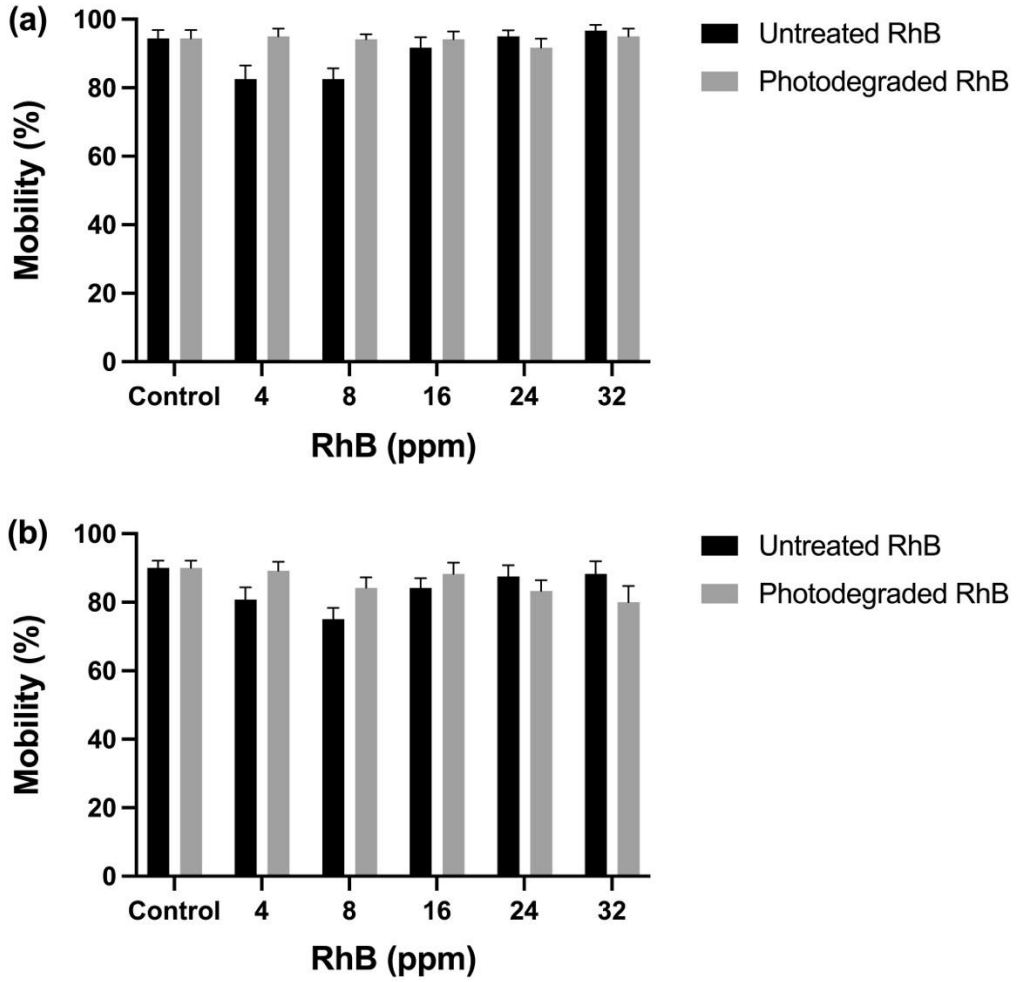

Figure 8: Mobility of *Artemia franciscana* larvae after 24 h (a) and 48 h (b) of exposure to untreated RhB and photodegraded RhB. Data are expressed as mean ± SEM.

4. Conclusion

Here, we demonstrate the application of the DAC technique for the synthesis of new TiO_2/g-C_3N_4 heterojunctions, confirmed by TEM and XRD analysis. The synthesis methodology has proved to be effective for producing heterojunctions with greater absorption in the visible light region, when compared to the precursors. XPS data shows a $Ti^{4+} \rightarrow Ti^{3+}$ reduction during the synthesis, leading to the formation of oxygen vacancies, improving the photocatalytic process. Photodegradation experiments indicate a mass ratio of 1:0.1 as optimal for the highest photocatalytic performance in RhB and MB degradation. Radical trapping experiments show the TiO_2/g-C_3N_4 (1.0/0.1) heterojunction functions via a Z-scheme mechanism. All RhB photodegradation products shown no ecotoxicity against *A. franciscana* larvae.

Supporting Information

The Supporting Information is available free of charge and shows additional data such as infrared spectra, UV-VIS spectra, and XRD details.

Acknowledgements

The Prof. Dr. Fausthon F. da Silva gratefully acknowledge to a CAPES-PrInt-UFPB (N◦ 8881.311774/2018-01 and 88887.569104/2020-00), CNPq (406804/2022-2 and 303521/2022-8) and National Institute of Science and Technology on Molecular Sciences (INCT-CiMol) for the financial support.

Conflict of Interest

The authors declare that they have no known competing financial interests or personal relationships that could have appeared to influence the work reported in this paper.

CRediT authorship contribution statement

Fausthon Fred da Silva: Conceptualization, Methodology, Validation, Resources, Visualization, Investigation, Writing original draft, Formal analysis, Project administration.

André L. Menezes de Oliveira: Methodology, Validation, Visualization, Investigation, Writing original draft and Formal analysis.

Thayná Carla Barbosa de Araújo: Methodology, Validation, Visualization, Investigation, Writing original draft and Formal analysis.

Luis Fernando Marques-Santos: Methodology, Validation, Resources, Visualization, Investigation and Writing original draft and Formal analysis.

Bo Su: Conceptualization, Methodology, Validation, Resources, Visualization, Investigation, Funding acquisition, Writing original draft, Formal analysis, and Project administration.

References

[1] L. Zhou, L. Wang, J. Zhang, J. Lei, Y. Liu, The preparation, and applications of g-C3N4/TiO2 heterojunction catalysts—a review, Research on Chemical Intermediates 43 (2017) 2081–2101. https://doi.org/10.1007/s11164-016-2748-8.

[2] R. Acharya, K. Parida, A review on TiO2/g-C3N4 visible-light-responsive photocatalysts for sustainable energy generation and environmental remediation, J Environ Chem Eng 8 (2020). https://doi.org/10.1016/j.jece.2020.103896.

[3] W. Jiang, Z. Li, C. Liu, D. Wang, G. Yan, B. Liu, G. Che, Enhanced visible-light-induced photocatalytic degradation of tetracycline using BiOI/MIL-125(Ti) composite photocatalyst, J Alloys Compd 854 (2021) 157166. https://doi.org/10.1016/j.jallcom.2020.157166.

[4] J. Fu, J. Yu, C. Jiang, B. Cheng, g-C3N4-Based Heterostructured Photocatalysts, Adv Energy Mater 8 (2018) 1701503. https://doi.org/10.1002/aenm.201701503.

[5] W.-J. Ong, L.-L. Tan, Y.H. Ng, S.-T. Yong, S.-P. Chai, Graphitic Carbon Nitride (g-C_3N_4)-Based Photocatalysts for Artificial Photosynthesis and Environmental Remediation: Are We a Step Closer To Achieving Sustainability?, Chem Rev 116 (2016) 7159–7329. https://doi.org/10.1021/acs.chemrev.6b00075.

[6] S. Hu, X. Qu, J. Bai, P. Li, Q. Li, F. Wang, L. Song, Effect of Cu(I)-N Active Sites on the N2 Photofixation Ability over Flowerlike Copper-Doped g-C3N4 Prepared via a Novel Molten Salt-Assisted Microwave Process: The Experimental and Density Functional Theory Simulation Analysis, ACS Sustain Chem Eng 5 (2017) 6863–6872. https://doi.org/10.1021/acssuschemeng.7b01089.

[7] S. Hu, F. Li, Z. Fan, F. Wang, Y. Zhao, Z. Lv, Band gap-tunable potassium doped graphitic carbon nitride with enhanced mineralization ability, Dalton Transactions 44 (2014) 1084–1092. https://doi.org/10.1039/c4dt02658f.

[8] S. Hu, X. Qu, P. Li, F. Wang, Q. Li, L. Song, Y. Zhao, X. Kang, Photocatalytic oxygen reduction to hydrogen peroxide over copper doped graphitic carbon nitride hollow microsphere: The effect of Cu(I)-N active sites, Chemical Engineering Journal 334 (2018) 410–418. https://doi.org/10.1016/j.cej.2017.10.016.

[9] J. Zhao, L. Ma, H. Wang, Y. Zhao, J. Zhang, S. Hu, Novel band gap-tunable K-Na co-doped graphitic carbon nitride prepared by molten salt method, Appl Surf Sci 332 (2015) 625–630. https://doi.org/10.1016/j.apsusc.2015.01.233.

[10] S. Hu, L. Ma, J. You, F. Li, Z. Fan, G. Lu, D. Liu, J. Gui, Enhanced visible light photocatalytic performance of g-C 3 N 4 photocatalysts co-doped with iron and phosphorus, Appl Surf Sci 311 (2014) 164–171. https://doi.org/10.1016/j.apsusc.2014.05.036.

[11] R. Hao, G. Wang, C. Jiang, H. Tang, Q. Xu, In situ hydrothermal synthesis of g-C 3 N 4 /TiO 2 heterojunction photocatalysts with high specific surface area for Rhodamine B degradation, Appl Surf Sci 411 (2017) 400–410. https://doi.org/10.1016/j.apsusc.2017.03.197.

[12] Q. Tang, X. Meng, Z. Wang, J. Zhou, H. Tang, One-step electrospinning synthesis of TiO 2 /g-C 3 N 4 nanofibers with enhanced photocatalytic properties, Appl Surf Sci 430 (2018) 253–262. https://doi.org/10.1016/j.apsusc.2017.07.288.

[13] S. Ma, J. Xue, Y. Zhou, Z. Zhang, Z. Cai, D. Zhu, S. Liang, Facile fabrication of a mpg-C3N4/TiO2 heterojunction photocatalyst with enhanced visible light photoactivity toward organic pollutant degradation, RSC Adv 5 (2015) 64976–64982. https://doi.org/10.1039/c5ra10447e.

[14] X. Chen, J. Wei, R. Hou, Y. Liang, Z. Xie, Y. Zhu, X. Zhang, H. Wang, Growth of g-C3N4 on mesoporous TiO2 spheres with high photocatalytic activity under visible light irradiation, Appl Catal B 188 (2016) 342–350. https://doi.org/10.1016/j.apcatb.2016.02.012.

[15] Z. Tong, D. Yang, T. Xiao, Y. Tian, Z. Jiang, Biomimetic fabrication of g-C3N4/TiO2 nanosheets with enhanced photocatalytic activity toward organic pollutant degradation, Chemical Engineering Journal 260 (2015) 117–125. https://doi.org/10.1016/j.cej.2014.08.072.

[16] N. Yang, G. Li, W. Wang, X. Yang, W.F. Zhang, Photophysical and enhanced daylight photocatalytic properties of N-doped TiO2/g-C3N4 composites, Journal of Physics and Chemistry of Solids 72 (2011) 1319–1324. https://doi.org/10.1016/j.jpcs.2011.07.028.

[17] J. Zhou, M. Zhang, Y. Zhu, Photocatalytic enhancement of hybrid C3N4/TiO2 prepared via ball milling method, Physical Chemistry Chemical Physics 17 (2015) 3647–3652. https://doi.org/10.1039/c4cp05173d.

[18] Y. Jiang, Y. Wang, K. Zhou, S. Ding, J. Yu, Influence of TiO2 conjunct with different g–C3N4 mass ratios on photocatalytic activity: visible and UV degradation of organic pollutant, Journal of Materials Science: Materials in Electronics 32 (2021) 28321–28334. https://doi.org/10.1007/s10854-021-07208-3.

[19] Q. Tay, X. Wang, X. Zhao, J. Hong, Q. Zhang, R. Xu, Z. Chen, Enhanced visible light hydrogen production via a multiple heterojunction structure with defect-engineered g-C3N4 and two-phase anatase/brookite TiO2, J Catal 342 (2016) 55–62. https://doi.org/10.1016/j.jcat.2016.07.007.

[20] G. Li, Y. Cai, X. Wang, L. Zhang, Q. Xie, P. Chen, C. Li, J. Sun, T. Li, L. Dong, Direct Z-scheme heterojunction rutile-TiO2/g-C3N4 catalyst constructed by solid grinding method for photocatalysis degradation, Chem Phys 559 (2022). https://doi.org/10.1016/j.chemphys.2022.111558.

[21] Y. Wang, J. Yu, W. Peng, J. Tian, C. Yang, Novel multilayer TiO2 heterojunction decorated by low g-C3N4 content and its enhanced photocatalytic activity under UV, visible and solar light irradiation, Sci Rep 9 (2019). https://doi.org/10.1038/s41598-019-42438-w.

[22] U. Massing, S. Cicko, V. Ziroli, Dual asymmetric centrifugation (DAC)-A new technique for liposome preparation, Journal of Controlled Release 125 (2008) 16–24. https://doi.org/10.1016/j.jconrel.2007.09.010.

[23] S. Agate, P. Tyagi, V. Naithani, L. Lucia, L. Pal, Innovating Generation of Nanocellulose from Industrial Hemp by Dual Asymmetric Centrifugation, ACS Sustain Chem Eng 8 (2020) 1850–1858. https://doi.org/10.1021/acssuschemeng.9b05992.

[24] J.W. Osborne, G.W. Ferguson, S.E. Sorensen, E.M. Gale, Operative dentistry and fixed partial prosthodontics, 1974.

[25] A.A. Barba, S. Bochicchio, A. Dalmoro, G. Lamberti, Lipid delivery systems for nucleic-acid-based-drugs: From production to clinical applications, Pharmaceutics 11 (2019). https://doi.org/10.3390/pharmaceutics11080360.

[26] L. Gao, X. Ji, K. Zhang, Z.W. Li, Y.K. Zhang, Influence of mixing process on the mechanical and tribological properties of PTFE composites, Plastics, Rubber and Composites 50 (2021) 146–152. https://doi.org/10.1080/14658011.2020.1855388.

[27] M.D. Womble, J. Herbsommer, Y.J. Lee, J.W.P. Hsu, Effects of TiO2 nanoparticle size and concentration on dielectric properties of polypropylene nanocomposites, J Mater Sci 53 (2018) 9149–9159. https://doi.org/10.1007/s10853-018-2223-6.

[28] M.A. Raza, A. Westwood, A. Brown, N. Hondow, C. Stirling, Characterisation of graphite nanoplatelets and the physical properties of graphite nanoplatelet/silicone composites for thermal interface applications, Carbon N Y 49 (2011) 4269–4279. https://doi.org/10.1016/j.carbon.2011.06.002.

[29] A. Alrahlah, R. Khan, F. Vohra, I.M. Alqahtani, A.A. Alruhaymi, S. Haider, A.-B. Al-Odayni, W.S. Saeed, H.C.A. Murthy, L.S. Bautista, Influence of the Physical Inclusion of ZrO2/TiO2 Nanoparticles on Physical, Mechanical, and Morphological Characteristics of PMMA-Based Interim Restorative Material, Biomed Res Int 2022 (2022) 1–11. https://doi.org/10.1155/2022/1743019.

[30] M.D. Womble, J. Herbsommer, Y.-J. Lee, J. Hsu, Understanding the source of dielectric loss in Titania/polypropylene nanocomposites up to 220 GHz, in: Optical Interconnects XVII, SPIE, 2017: p. 1010908. https://doi.org/10.1117/12.2250346.

[31] A. Alrahlah, R. Khan, F. Vohra, I.M. Alqahtani, A.A. Alruhaymi, S. Haider, A.B. Al-Odayni, W.S. Saeed, H.C.A. Murthy, L.S. Bautista, Influence of the Physical Inclusion of ZrO2/TiO2Nanoparticles on Physical, Mechanical, and Morphological Characteristics of PMMA-Based Interim Restorative Material, Biomed Res Int 2022 (2022). https://doi.org/10.1155/2022/1743019.

[32] F.F. da Silva, B. Su, Dual asymmetric centrifugation as a new tool to prepare TiO2/S-g-C3N4 heterojunctions with high photocatalytic performance, Ceram Int 49 (2023) 13265–13270. https://doi.org/10.1016/j.ceramint.2023.01.109.

[33] S. Selvinsimpson, S. Eva Gnana Dhana Rani, A. Ganesh Kumar, R. Rajaram, I. Sharmila Lydia, Y. Chen, Photocatalytic activity of SnO2/Fe3O4 nanocomposites and the toxicity assessment of Vigna radiata, Artemia salina and Danio rerio in the photodegraded solution, Environ Res 195 (2021) 110787. https://doi.org/10.1016/j.envres.2021.110787.

[34] A.J.T. Machado, B. Mataribu, C. Serrão, L. da Silva Silvestre, D.F. Farias, E. Bergami, I. Corsi, L.F. Marques-Santos, Single and combined toxicity of amino-functionalized polystyrene nanoparticles with potassium dichromate and copper sulfate on brine shrimp Artemia franciscana larvae, Environmental Science and Pollution Research 28 (2021) 45317–45334. https://doi.org/10.1007/s11356-021-13907-5.

[35] M. Kos, A. Kahru, D. Drobne, S. Singh, G. Kalčíková, D. Kühnel, R. Rohit, A.Ž. Gotvajn, A. Jemec, A case study to optimise and validate the brine shrimp Artemia franciscana immobilisation assay with silver nanoparticles: The role of harmonisation, Environmental Pollution 213 (2016) 173–183. https://doi.org/10.1016/j.envpol.2016.02.015.

[36] F. Fina, S.K. Callear, G.M. Carins, J.T.S. Irvine, Structural investigation of graphitic carbon nitride via XRD and neutron diffraction, Chemistry of Materials 27 (2015) 2612–2618. https://doi.org/10.1021/acs.chemmater.5b00411.

[37] W. Li, C. Li, B. Chen, X. Jiao, D. Chen, Facile synthesis of sheet-like N-TiO2/g-C3N4 heterojunctions with highly enhanced and stable visible-light photocatalytic activities, RSC Adv 5 (2015) 34281–34291. https://doi.org/10.1039/c5ra04100g.

[38] K. Kondo, N. Murakami, C. Ye, T. Tsubota, T. Ohno, Development of highly efficient sulfur-doped TiO2 photocatalysts hybridized with graphitic carbon nitride, Appl Catal B 142–143 (2013) 362–367. https://doi.org/10.1016/j.apcatb.2013.05.042.

[39] H. Yan, H. Yang, TiO 2 -g-C 3 N 4 composite materials for photocatalytic H 2 evolution under visible light irradiation, J Alloys Compd 509 (2011). https://doi.org/10.1016/j.jallcom.2010.09.201.

[40] L. Liu, D. Ma, H. Zheng, X. Li, M. Cheng, X. Bao, Synthesis and characterization of microporous carbon nitride, Microporous and Mesoporous Materials 110 (2008) 216–222. https://doi.org/10.1016/j.micromeso.2007.06.012.

[41] K. Gibson, J. Glaser, E. Milke, M. Marzini, S. Tragl, M. Binnewies, H.A. Mayer, H.J. Meyer, Preparation of carbon nitride materials by polycondensation of the single-source precursor aminodichlorotriazine (ADCT), Mater Chem Phys 112 (2008) 52–56. https://doi.org/10.1016/j.matchemphys.2008.05.007.

[42] M. Li, B. Dong, Z. Chang, H. Dang, S. Ma, W. Li, Synthesis of TiO2/g-C3N4 Photocatalyst with Recovered TiO2 from Spent SCR Catalyst for Photodegrading Rhodamine B, Waste Biomass Valorization (2022). https://doi.org/10.1007/s12649-022-01917-4.

[43] N. Lu, C. Wang, B. Sun, Z. Gao, Y. Su, Fabrication of TiO2-doped single layer graphitic-C3N4 and its visible-light photocatalytic activity, Sep Purif Technol 186 (2017) 226–232. https://doi.org/10.1016/j.seppur.2017.06.008.

[44] Y. Xu, S.P. Gao, Band gap of C3N4 in the GW approximation, Int J Hydrogen Energy 37 (2012) 11072–11080. https://doi.org/10.1016/j.ijhydene.2012.04.138.

[45] R. Sanjinés, H. Tang, H. Berger, F. Gozzo, G. Margaritondo, F. Lévy, Electronic structure of anatase TiO2 oxide, J Appl Phys 75 (1994) 2945–2951. https://doi.org/10.1063/1.356190.

[46] J. Ma, X. Tan, T. Yu, X. Li, Fabrication of g-C3N4/TiO2 hierarchical spheres with reactive {001} TiO2 crystal facets and its visible-light photocatalytic activity, Int J Hydrogen Energy 41 (2016) 3877–3887. https://doi.org/10.1016/j.ijhydene.2015.12.191.

[47] H. Wang, H. Li, Z. Chen, J. Li, X. Li, P. Huo, Q. Wang, TiO2 modified g-C3N4 with enhanced photocatalytic CO2 reduction performance, Solid State Sci 100 (2020). https://doi.org/10.1016/j.solidstatesciences.2019.106099.

[48] S. Chaitaworn, O. Mekasuwandumrong, P. Praserthdam, Impact of Oxygen Vacancy on the Photocatalytic Selective Hydrogenation of 3-Nitrostyrene via Calcination of TiO_2, IOP Conf Ser Mater Sci Eng 559 (2019) 012015. https://doi.org/10.1088/1757-899X/559/1/012015.

[49] C. Foo, Y. Li, K. Lebedev, T. Chen, S. Day, C. Tang, S.C.E. Tsang, Characterisation of oxygen defects and nitrogen impurities in TiO2 photocatalysts using variable-temperature X-ray powder diffraction, Nat Commun 12 (2021) 661. https://doi.org/10.1038/s41467-021-20977-z.

[50] K. Li, Z. Huang, X. Zeng, B. Huang, S. Gao, J. Lu, Synergetic Effect of Ti3+ and Oxygen Doping on Enhancing Photoelectrochemical and Photocatalytic Properties of TiO2/g-C3N4

Heterojunctions, ACS Appl Mater Interfaces 9 (2017) 11577–11586. https://doi.org/10.1021/acsami.6b16191.

[51] Y. Zhang, Q. Pan, G. Chai, M. Liang, G. Dong, Q. Zhang, J. Qiu, Synthesis and luminescence mechanism of multicolor-emitting g-C3N4 nanopowders by low temperature thermal condensation of melamine, Sci Rep 3 (2013) 1943. https://doi.org/10.1038/srep01943.

[52] W. Shi, W.X. Fang, J.C. Wang, X. Qiao, B. Wang, X. Guo, pH-controlled mechanism of photocatalytic RhB degradation over g-C3N4 under sunlight irradiation, Photochemical and Photobiological Sciences 20 (2021) 303–313. https://doi.org/10.1007/s43630-021-00019-9.

[53] C. Yao, X. Wang, W. Zhao, T. Li, Y. He, X. Ran, L. Guo, Probing the facet-dependent intermediate in the visible-light degradation of RhB by carbon-coated anatase TiO2 nanoparticles, J Alloys Compd 846 (2020). https://doi.org/10.1016/j.jallcom.2020.156335.

[54] S. Gonuguntla, R. Kamesh, U. Pal, D. Chatterjee, Dye sensitization of TiO2 relevant to photocatalytic hydrogen generation: Current research trends and prospects, Journal of Photochemistry and Photobiology C: Photochemistry Reviews 57 (2023) 100621. https://doi.org/10.1016/j.jphotochemrev.2023.100621.

[55] H. Guo, Y. Ke, D. Wang, K. Lin, R. Shen, J. Chen, W. Weng, Efficient adsorption and photocatalytic degradation of Congo red onto hydrothermally synthesized NiS nanoparticles, Journal of Nanoparticle Research 15 (2013). https://doi.org/10.1007/s11051-013-1475-y.

[56] F. Aisien, A.N. Amenaghawon, F.A. Aisien, N.A. Amenaghawon, O.I. Urhobotie, Potential application of a locally sourced photocatalyst for the photocatalytic decolourisation of methyl orange in aqueous solution, 2015.

[57] M.S. Athar, M. Danish, M. Muneer, Fabrication of visible light-responsive dual Z-Scheme (α-Fe2O3/CdS/g-C3N4) ternary nanocomposites for enhanced photocatalytic performance and adsorption study in aqueous suspension, J Environ Chem Eng 9 (2021). https://doi.org/10.1016/j.jece.2021.105754.

[58] H. Ashrafi, M. Akhond, G. Absalan, Adsorption and photocatalytic degradation of aqueous methylene blue using nanoporous carbon nitride, J Photochem Photobiol A Chem 396 (2020). https://doi.org/10.1016/j.jphotochem.2020.112533.

[59] P. Mishra, L. Acharya, K. Parida, A comparison study between novel ternary retrieval NiFe2O4@P-doped g-C3N4and Fe3O4@P-doped g-C3N4nanocomposite in the field of photocatalysis, H2energy production and super capacitive property, in: Mater Today Proc, Elsevier Ltd, 2021: pp. 281–288. https://doi.org/10.1016/j.matpr.2020.05.764.

[60] Y. Jiang, Y. Wang, K. Zhou, S. Ding, J. Yu, Influence of TiO2 conjunct with different g–C3N4 mass ratios on photocatalytic activity: visible and UV degradation of organic pollutant, Journal of Materials Science: Materials in Electronics 32 (2021) 28321–28334. https://doi.org/10.1007/s10854-021-07208-3.

[61] K. Li, Z. Huang, X. Zeng, B. Huang, S. Gao, J. Lu, Synergetic Effect of Ti3+ and Oxygen Doping on Enhancing Photoelectrochemical and Photocatalytic Properties of TiO2/g-C3N4 Heterojunctions, ACS Appl Mater Interfaces 9 (2017) 11577–11586. https://doi.org/10.1021/acsami.6b16191.

[62] X. Lu, Q. Wang, D. Cui, Preparation and Photocatalytic Properties of g-C 3 N 4 /TiO 2 Hybrid Composite, 2010. https://doi.org/10.1016/S1005-0302(10)60149-1.

[63] D. Baranowska, T. Kędzierski, M. Dworczak, M. Baca, E. Mijowska, B. Zielińska, Bifunctional catalyst based on molecular structure: Spherical mesoporous TiO2 and gCN for photocatalysis, Mater Res Bull 146 (2022). https://doi.org/10.1016/j.materresbull.2021.111608.

[64] Y. Jiang, H. Zhang, Q. Chen, Z. Sun, L. Zeng, Constructing Z-scheme carbon-rich carbon nitride/TiO2 photocatalyst for improved photocatalytic activity, Applied Surface Science Advances 9 (2022). https://doi.org/10.1016/j.apsadv.2022.100238.

[65] C. Zhou, N.F. Ye, X.H. Yan, J.J. Wang, J.M. Pan, D.F. Wang, Q. Wang, J.X. Zu, X.N. Cheng, Construction of hybrid Z-scheme graphitic C3N4/reduced TiO2 microsphere with visible-light-driven photocatalytic activity, Journal of Materiomics 4 (2018) 238–246. https://doi.org/10.1016/j.jmat.2018.04.002.

[66] S. Luan, D. Qu, L. An, W. Jiang, X. Gao, S. Hua, X. Miao, Y. Wen, Z. Sun, Enhancing photocatalytic performance by constructing ultrafine TiO2 nanorods/g-C3N4 nanosheets heterojunction for water treatment, Sci Bull (Beijing) 63 (2018) 683–690. https://doi.org/10.1016/j.scib.2018.04.002.

[67] M. Song, M. Li, Y. Guo, X. Huang, S. Wang, L. Ren, L. Li, Y. Wu, Facile fabrication of ordered assembled TiO2/g-C3N4 nanosheets with enhanced photocatalytic activity, Ceram Int 47 (2021) 15594–15603. https://doi.org/10.1016/j.ceramint.2021.02.129.

[68] X. Zhang, L. Li, Y. Zeng, F. Liu, J. Yuan, X. Li, Y. Yu, X. Zhu, Z. Xiong, H. Yu, Y. Xie, TiO2/Graphitic Carbon Nitride Nanosheets for the Photocatalytic Degradation of Rhodamine B under Simulated Sunlight, ACS Appl Nano Mater 2 (2019) 7255–7265. https://doi.org/10.1021/acsanm.9b01739.

[69] L. Ma, G. Wang, C. Jiang, H. Bao, Q. Xu, Synthesis of core-shell TiO 2 @g-C 3 N 4 hollow microspheres for efficient photocatalytic degradation of rhodamine B under visible light, Appl Surf Sci 430 (2018) 263–272. https://doi.org/10.1016/j.apsusc.2017.07.282.

[70] H. Xiao, T. Wang, Study on the catalytic activities of g-C3N4@TiO2 hollow microspheres under UV–visible light, Journal of Materials Science: Materials in Electronics 32 (2021) 5104–5115. https://doi.org/10.1007/s10854-021-05244-7.

[71] L. Gu, J. Wang, Z. Zou, X. Han, Graphitic-C3N4-hybridized TiO2 nanosheets with reactive {001} facets to enhance the UV- and visible-light photocatalytic activity, J Hazard Mater 268 (2014) 216–223. https://doi.org/10.1016/j.jhazmat.2014.01.021.

[72] M. Sharma, S. Vaidya, A.K. Ganguli, Enhanced photocatalytic activity of g-C3N4-TiO2 nanocomposites for degradation of Rhodamine B dye, J Photochem Photobiol A Chem 335 (2017) 287–293. https://doi.org/10.1016/j.jphotochem.2016.12.002.

[73] Y. Jiang, F. Li, Y. Liu, Y. Hong, P. Liu, L. Ni, Construction of TiO2 hollow nanosphere/g-C3N4 composites with superior visible-light photocatalytic activity and mechanism insight, Journal of Industrial and Engineering Chemistry 41 (2016) 130–140. https://doi.org/10.1016/j.jiec.2016.07.013.

[74] X. Liu, J. Chen, L. Yang, S. Yun, M. Que, H. Zheng, Y. Zhao, T. Yang, Z. Liu, 2D/2D g-C3N4/TiO2 with exposed (001) facets Z-Scheme composites accelerating separation of interfacial charge

and visible photocatalytic degradation of Rhodamine B, Journal of Physics and Chemistry of Solids 160 (2022). https://doi.org/10.1016/j.jpcs.2021.110339.

[75] S.T. Liu, A.B. Zhang, K.K. Yan, Y. Ye, X.G. Chen, Microwave-enhanced catalytic degradation of methylene blue by porous MFe2O4 (M = Mn, Co) nanocomposites: Pathways and mechanisms, Sep Purif Technol 135 (2014) 35–41. https://doi.org/10.1016/j.seppur.2014.07.049.

[76] N. Boonprakob, N. Wetchakun, S. Phanichphant, D. Waxler, P. Sherrell, A. Nattestad, J. Chen, B. Inceesungvorn, Enhanced visible-light photocatalytic activity of g-C3N4/TiO2 films, J Colloid Interface Sci 417 (2014) 402–409. https://doi.org/10.1016/j.jcis.2013.11.072.

[77] M. Fu, J. Liao, F. Dong, H. Li, H. Liu, Growth of g-C3N4 layer on commercial TiO2 for enhanced visible light photocatalytic activity, J Nanomater 2014 (2014). https://doi.org/10.1155/2014/869094.

[78] K. Sridharan, E. Jang, T.J. Park, Novel visible light active graphitic C3N4-TiO2 composite photocatalyst: Synergistic synthesis, growth and photocatalytic treatment of hazardous pollutants, Appl Catal B 142–143 (2013) 718–728. https://doi.org/10.1016/j.apcatb.2013.05.077.

[79] H. Liu, D. Yu, T. Sun, H. Du, W. Jiang, Y. Muhammad, L. Huang, Fabrication of surface alkalinized g-C 3 N 4 and TiO 2 composite for the synergistic adsorption-photocatalytic degradation of methylene blue, Appl Surf Sci 473 (2019) 855–863. https://doi.org/10.1016/j.apsusc.2018.12.162.

[80] X. Yuan, M. Sun, Y. Yao, X. Lin, J. Shi, N/Ti3+-codoped triphasic TiO2/g-C3N4 heterojunctions as visible-light photocatalysts for the degradation of organic contaminants, New Journal of Chemistry 43 (2019) 2665–2675. https://doi.org/10.1039/c8nj04595j.

[81] M. Faisal, A.A. Ismail, F.A. Harraz, S.A. Al-Sayari, A.M. El-Toni, A.E. Al-Salami, M.S. Al-Assiri, Fabrication of highly efficient TiO2/C3N4 visible light driven photocatalysts with enhanced photocatalytic activity, J Mol Struct 1173 (2018) 428–438. https://doi.org/10.1016/j.molstruc.2018.07.014.

[82] J. Qiu, Y. Feng, X. Zhang, X. Zhang, M. Jia, J. Yao, Facile stir-dried preparation of g-C3N4/TiO2 homogeneous composites with enhanced photocatalytic activity, RSC Adv 7 (2017) 10668–10674. https://doi.org/10.1039/c7ra00050b.

[83] Z. Liu, H. Zheng, H. Yang, L. Hao, L. Wen, T. Xu, S. Wu, Mpg-C3N4/anatase TiO2 with reactive {001} facets composites to enhance the photocatalytic activity of organic dye degradation, RSC Adv 6 (2016) 54215–54225. https://doi.org/10.1039/c6ra06730a.

[84] M.A.F. Md Fauzi, M.H. Razali, M.U. Osman, B. Mohd Azam, Synthesis and characterisation of TiO2/g-C3N4 as photocatalyst for photodegradation of dyes, phenol and caffeine, Advances in Materials and Processing Technologies (2022). https://doi.org/10.1080/2374068X.2022.2076976.

[85] D.P.T. Duong, T. Doan Van, P. Bui Dai, T.N. Nguyen Tran, T.N.U. Nguyen, T. Cao Minh, T.K. Nguyen, Y.S. Kim, V. Pham Van, Excellent visible light-driven photocatalytic performance and band alignment of g-C3N4/TiO2 nanotube heterostructures, Mater Res Express 6 (2019). https://doi.org/10.1088/2053-1591/ab2021.

[86] M.H. Razali, M.A.F. Md Fauzi, B. Mohd Azam, M. Yusoff, g-C3N4/TiO2 nanocomposite photocatalyst for methylene blue photodegradation under visible light, Applied Nanoscience (Switzerland) (2022). https://doi.org/10.1007/s13204-021-02328-y.

[87] K. Li, S. Gao, Q. Wang, H. Xu, Z. Wang, B. Huang, Y. Dai, J. Lu, In-situ-reduced synthesis of Ti3+ self-doped TiO2/g-C3N4 heterojunctions with high photocatalytic performance under LED light irradiation, ACS Appl Mater Interfaces 7 (2015) 9023–9030. https://doi.org/10.1021/am508505n.

[88] Y.R. Girish, Udayabhanu, G. Alnaggar, A. Hezam, M.B. Nayan, G. Nagaraju, K. Byrappa, Facile and rapid synthesis of solar-driven TiO2/g-C3N4 heterostructure photocatalysts for enhanced photocatalytic activity, Journal of Science: Advanced Materials and Devices 7 (2022). https://doi.org/10.1016/j.jsamd.2022.100419.

[89] S. Sun, M. Sun, Y. Fang, Y. Wang, H. Wang, One-step in situ calcination synthesis of g-C3N4/N-TiO2 hybrids with enhanced photoactivity, RSC Adv 6 (2016) 13063–13071. https://doi.org/10.1039/c5ra26700e.

[90] Y. Wu, S. Chen, J. Zhao, X. Yue, W. Deng, Y. Li, C. Wang, Mesoporous graphitic carbon nitride and carbon-TiO2 hybrid composite photocatalysts with enhanced photocatalytic activity under visible light irradiation, J Environ Chem Eng 4 (2016) 797–807. https://doi.org/10.1016/j.jece.2015.10.023.

[91] C. Li, Z. Sun, Y. Xue, G. Yao, S. Zheng, A facile synthesis of g-C3N4/TiO2 hybrid photocatalysts by sol-gel method and its enhanced photodegradation towards methylene blue under visible light, Advanced Powder Technology 27 (2016) 330–337. https://doi.org/10.1016/j.apt.2016.01.003.

[92] X. Li, Q. Luo, L. Han, F. Deng, Y. Yang, F. Dong, Enhanced photocatalytic degradation and H2 evolution performance of N[sbnd]CDs/S-C3N4 S-scheme heterojunction constructed by π-π conjugate self-assembly, J Mater Sci Technol 114 (2022) 222–232. https://doi.org/10.1016/j.jmst.2021.10.030.

[93] D.A. Olmedo, Y. Vasquez, J.A. Morán, E.G. De León, C. Caballero-George, P.N. Solís, Understanding the *Artemia Salina* (Brine Shrimp) Test: Pharmacological Significance and Global Impact, Comb Chem High Throughput Screen 27 (2024) 545–554. https://doi.org/10.2174/1386207326666230703095928.

[94] B.S. Nunes, F.D. Carvalho, L.M. Guilhermino, G. Van Stappen, Use of the genus Artemia in ecotoxicity testing, Environmental Pollution 144 (2006) 453–462. https://doi.org/10.1016/j.envpol.2005.12.037.

[95] G. Libralato, E. Prato, L. Migliore, A.M. Cicero, L. Manfra, A review of toxicity testing protocols and endpoints with Artemia spp., Ecol Indic 69 (2016) 35–49. https://doi.org/10.1016/j.ecolind.2016.04.017.